Industrially Compatible Fabrication Process of Perovskite-Based Mini-Modules Coupling Sequential Slot-Die Coating and Chemical Bath Deposition

Iwan Zimmermann, Marion Provost, Salim Mejaouri, Marc Al Atem, Alexandre Blaizot, Aurélien Duchatelet, Stéphane Collin, Jean Rousset

Industrially Compatible Fabrication Process of Perovskite-Based Mini-Modules Coupling Sequential Slot-Die Coating and Chemical Bath Deposition

Iwan Zimmermann,[#,] Marion Provost,[#] Salim Mejaouri,[†] Marc Al Atem,[#] Alexandre Blaizot,[#] Aurélien Duchatelet,[†] Stéphane Collin[‡] and Jean Rousset[†,#]*

[#]Institut Photovoltaïque d'Île-de-France (IPVF). 18 Boulevard Thomas Gobert, Palaiseau 91120, France.

[†]EDF R&D, 7 Boulevard Gaspard Monge, 91120 Palaiseau, France

[‡]CNRS, Université Paris-Saclay, C2N, Centre de Nanosciences et de Nanotechnologies 10 Boulevard Thomas Gobert, 91120 Palaiseau, France

Corresponding Author

*Iwan Zimmermann. E-Mail: iwan.zimmermann@ipvf.fr

To upscale the emerging perovskite photovoltaic technology to larger size modules, industrially relevant deposition techniques need to be developed. In this work the deposition of tin oxide used as electron extraction layer is established using chemical bath deposition (CBD), a low-cost and solution-based fabrication process. Applying this simple low-temperature deposition method, highly homogeneous SnO_2 films are obtained in a reproducible manner. Moreover, the perovskite layer is prepared by sequentially slot-die-coating on top of the n-type contact. The symbiosis of these two industrially relevant deposition techniques allows for the growth of high-quality dense

perovskite layers with large grains. The uniformity of the perovskite film is further confirmed by SEM/STEM analysis coupled with EDX and cathodoluminescence measurements allowing to probe the elemental composition at the nano-scale. Perovskite solar cells fabricated from CBD SnO_2, and slot-die coated perovskite show power conversion efficiencies up to 19.2 %. Furthermore, mini-modules with an aperture area of 40 cm^2 demonstrate efficiencies of 17 % (18.1 % on active area).

TOC GRAPHICS

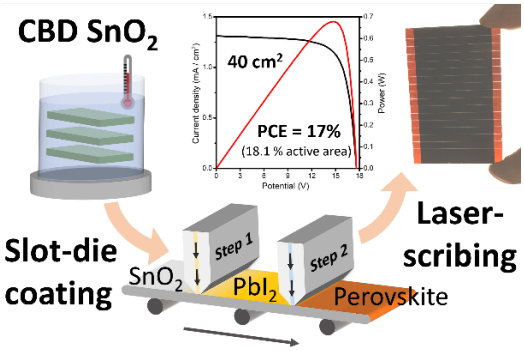

Over the last two decades, perovskite solar cells (PSC) have emerged as promising alternative thin film photovoltaic technology, with certified power conversion efficiencies already reaching beyond 25 %.[1–3] Organic- inorganic hybrid perovskites have stunning properties to be used as solar cell materials, including a high absorption coefficient in the visible range,[4] long carrier diffusion lengths[5,6] as well as low intrinsic material defect densities.[7] Furthermore, PSCs can be fabricated using low temperature solution processing techniques combined with low cost materials. The manufacturing of PCSs is therefore compatible with well-known industrial wet deposition techniques such as slot-die coating,[8,9] blade coating,[10–13] spray coating,[14] or ink-jet printing[15] in the quest of up-scaling the PSC technology to larger device areas. Up-scaling of PSCs is indeed a

major hurdle to overcome in making the perovskite technology commercially viable. Despite small laboratory devices reaching outstanding power conversion efficiencies, perovskite modules are lagging significantly behind in obtaining comparable performances. While laboratory cells fabricated by spin-coating have been certified at 25.5%,[2] small modules (~800 cm^2) certified by Panasonic are at 17.9%.[16] This gap in performance outlines the need of developing suitable large scale deposition methods for both the perovskite material as well as the involved charge extracting layers. Chemical bath deposition (CBD) has been applied for the deposition of compact TiO_2 and SnO_2 layers that are commonly used as n-type materials in a PSC with an n-i-p device architecture.[17,18] CBD is an inexpensive deposition method that can produce highly homogeneous layers on large areas at low temperatures. CBD has previously been employed at the industrial scale to produce CdS and ZnS buffer layers in CGIS photovoltaic modules.[19] Due to the relatively slow deposition rates, an industrial CBD process has to be performed in parallel coating a large number of conductive oxide plates simultaneously. Recently, the deposition of SnO_2 using CBD has shown outstanding results for PSCs in terms of device efficiency (> 25 %) as well as stability on both small cells,[3,20,21] and on mini-modules.[22] This level of performance clearly demonstrates that SnO_2 is very well suited for being implemented into a perovskite device, however the chemical mechanism that drives its deposition remains unclear. A deeper understanding of the different phenomena that rule the SnO_2 growth by CBD is needed to get an accurate control over the film quality and its optimal thickness. On the other hand, slot-die coating is a well-established industrial solution-based coating technique for deposition of uniform layers on large surfaces and therefore a method of choice for the perovskite deposition at the large scale. Thereby various quenching methods such as vacuum quenching[23], air-blading[24,25] or flash IR-heating[26] are used to induce a controlled perovskite crystallization for uniform film formation. Furthermore, sequential slot-die

deposition has been employed for high quality slot-die coated perovskite films.[27,28] Finally, a smart module design using suitable scribing techniques need to be closely adapted to ensure high efficiency and stability at the large scale. The relatively low conductivity in of transparent conductive oxides such as FTO and ITO used as substrate to grow the perovskite stack, limits the practical size of a single PSC device due to the increasing series resistance that scales approximately linear with the width of the PSC device. Laser ablation with P1, P2 and P3 scribing steps is the most widely used approach to fabricate PSC modules by connecting individual perovskite cells in series. Recent development in PSC module fabrication includes the optimization of the module interconnection by minimizing the loss of active area (dead area) from the scribing process as well as the reduction of electrical losses due to non-ideal interconnection (P2) within the modules. Such improvements are tackled by tuning the laser power as well as scribing width, which allows for precise control on material ablation, and at the same time limiting the material damage caused to the perovskite module.[29,30]

In this work we investigate the use of chemical bath deposition (CBD) for uniform deposition of tin oxide (SnO_2) as planar electron transport layer (ETL) on up to 10 cm x 10 cm substrates. The deposition mechanism is analyzed using in-situ quartz crystal micro balance measurements. Notably, we confirm the pivotal role of the dissolved oxygen, as oxidizing agent to produce Sn(IV), in the CBD process. The performance of the SnO_2 layers is evaluated fabricating PSC devices employing triple cation perovskite deposited by sequential slot-die coating. Sequential slot-die coating is presented as a suitable mean of depositing homogeneous perovskite films on up to 10 x 10 cm^2 large substrates. The growth of the perovskite layer on the CBD-SnO_2 is further analyzed performing STEM and SEM measurements probing both the cross-section and perovskite surface. Coupled with EDS and cathodoluminescence these experiments give insight on the morphology

combined with optoelectronic properties and the elemental distribution within the PSC at the local scale. Finally, power conversion efficiencies of up to 19.2% for small laboratory devices and 17% (18.1% on active area) for mini-modules with an aperture area of 40 cm^2 are presented.

Chemical bath deposition (CBD) of tin oxide (SnO_2) was performed utilizing $SnCl_2 \cdot 2H_2O$ as the tin precursor compound in an acidic aqueous solution (pH ~1.8) containing urea and mercaptoacetic acid as an additive (Figure 1a).

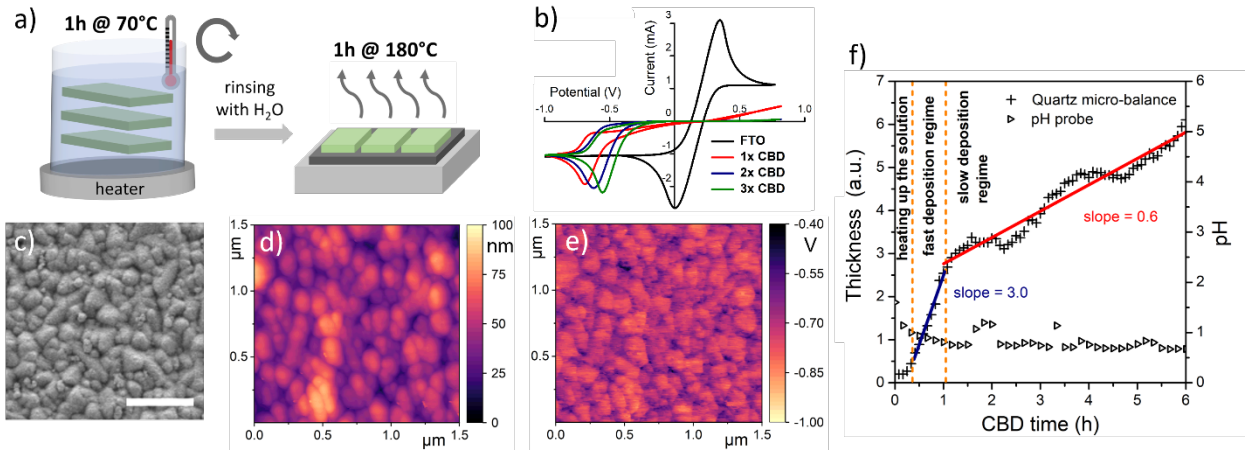

Figure 1 Growth of SnO_2 on FTO substrates via chemical bath deposition (CBD). a) schematic illustration of the CBD process, b) Cyclic Voltammetry on SnO_2 layers grown on FTO, probing the hole blocking capabilities. c) SEM top view image, d) AFM topology and e) KPFM surface potential of SnO_2 grown on FTO after two deposition cycles. f) Evolution of the pH and deposition rate of SnO_2 measured using a quartz micro balance during the CBD.

The deposition time was 1h during which the solution turned from clear transparent to murky, indicating the precipitation of solid tin oxide species in the solution. The temperature of the CBD reactor is thereby maintained at 70°C. The desired SnO_2 thickness was achieved by repeating the CBD deposition process for multiple times. Finally, the substrates are rinsed with water and

annealed at 180°C for 1h. The optimal thickness was evaluated checking the hole-blocking ability of the deposited tin oxide using cyclic voltammetry as shown in Figure 1b. We found that a single CBD cycle, regardless of the reaction time, is not enough to obtain a sufficiently blocking SnO_2 layer, as significant leaking currents can be observed during the CV scans when positive voltages are applied. On the other hand, SnO_2 layers grown using 2 and 3 CBD cycles were found to both fully block holes and efficiently transfer electrons. Looking at SEM top view images, we could observe an improved coverage of the FTO layer using consecutive depositions but also an increased number of nanoparticle aggregates present on the surface with additional CBD cycles (Figure 1c and S1). The topology of SnO_2 layers on FTO after 2 CBD cycles was evaluated by atomic force microscopy (AFM). The measured roughness was in the range of 100 nm as shown in Figure 1d and is comparable to the one observed for a bare FTO surface. To further characterize this SnO_2 layer, we performed kelvin probe force microscopy (KPFM) as shown in Figure 1e. From the measured potential we were able to calculate a work function of ϕ=-4.87±0.11 eV for a SnO_2 layer after 2 depositions, which is very similar to the one found for 3 CBD cycles (ϕ=-4.8±0.11 eV). These values are comparable to what has been reported in the literature on sputtered SnO_x layers (ϕ=-4.75 eV)[31] and SnO_2 quantum dots (ϕ=-4.93 eV).[32] Remarkably, the measured surface potential of the SnO_2 layers after only one CBD cycle (Figure S2) was found to be very different from the one after 2 and 3 depositions. We attribute this shift in work function to ϕ=-4.34±0.15 eV to the very thin nature of the SnO_2 layer. Furthermore, a contribution from the underlaying FTO layer could be observed analyzing the intensity distribution of the KPFM image for 1 CBD cycle (Figure S2) which could explain the poor hole blocking ability of the SnO_2 layer due to incomplete coverage of the FTO. The deposition rate during the CBD was closely monitored in-situ using a quartz crystal micro-balance (QCM). The results from the QCM measurements were

interpreted qualitatively to understand the deposition mechanism as an exact calibration turned out to be difficult. Following the mass gain over time we can divide the growth of SnO_2 in 3 different deposition regimes as shown in Figure 1f. During the initial heating up of the solution no deposition is observed. We found that the deposition is starting at a bath temperature of around 50 °C that induces a fast deposition regime which lasts around 1h. During this time frame most of the deposition is happening and the transition from a clear to murky solution due to the precipitation of SnO_2 nanoparticles can be observed. From SEM/TEM cross-sectional images we estimated the accumulated thickness of the SnO_2 layer after 1h to be around 10 nm. Further continuing the CBD leads to a transition into a slow deposition regime with deposition rates being around 5 times lower than in the fast deposition window, as calculated from the slope of the accumulated thickness. Based on above mentioned results the deposition time of 1 h was found to be optimal in terms of deposition rate over time and therefore adapted for all further sample preparations within this work. The formation of SnO_2 nanoparticles in the CBD solution was confirmed by collecting the precipitate after the CBD reaction followed by further analysis by powder X-ray diffraction (XRD) (Figure S3). CBD processed SnO_2 layers turned out to be too thin or not crystalline enough to provide a well resolved XRD pattern. The broad XRD peaks from the dried powders indicate the formation of SnO_2 nanoparticles that crystalize in the SnO_2 cassiterite phase. Moreover, we found that the activation of the precursor solution plays an important role in the SnO_2 CBD process. Thus, precursor solutions were typically stored at 4°C for 3 days prior to use. We note that the solution can be stored for several weeks under this condition however precipitation of SnO_2 starts to occur after 1-2 days at room temperature. Without this preliminary step no SnO_2 precipitation could be observed during the CBD (Figure S4). We found that aging process allows for the controlled oxidation of part of the $SnCl_2$ to $Sn(OH)_4$, following the mechanism outlined in equation (1) as

suggested by the Pourbaix diagrams of the Sn/H_2O-Cl system[33]. Oxygen dissolved in the solution thereby acts as the oxidizing agent[34]. This was further confirmed by aging the solution under nitrogen atmosphere, after a careful sparging of the solution, as no deposition could be observed during the CBD in this case. Additionally, a small decrease in the pH before (pH=1.0) and after (pH=0.97) the aging process (no-diluted solution), can be attributed to the formation of HCl in (1). During the CBD reaction, the unstable $Sn(OH)_4$ hydroxide species in the activated solution further transform into solid SnO_2 at elevated temperatures (2). Urea also plays an important role in the CBD reaction as solutions containing no urea displayed a much slower precipitation of SnO_2 during the CBD reaction (Figure S4). We speculate that the addition of urea accelerates the precipitation of $Sn(OH)_4$ intermediates, which are less likely to precipitate at lower pH according to the Pourbaix diagram.

$$SnCl_2 + ½\ O_2 + 4\ H_2O \rightleftharpoons Sn(OH)_4(aq) + H_2O + 2\ HCl \quad (1)$$

$$Sn(OH)_4(aq)\ (heat) \rightarrow SnO_2(s) + 2\ H_2O \quad (2)$$

To confirm the precipitation of Sn(IV) at 70° into SnO_2 we performed a CBD reaction using a solution prepared from $SnCl_4$ as the tin precursor compound in water. We found the precipitation of SnO_2 is indeed possible without aging or addition of urea as confirmed by XRD analysis of the dried powders (Figure S3). As the reaction temperature of 70°C is below the reported decomposition temperature of urea, we do not expect urea to decompose in significant amounts during the deposition process. This is consistent following the pH of the CBD solution, using an in-situ pH probe. We note that with elevated reaction temperatures (>80°C) the decomposition of urea leads to an increase in pH during the CBD reaction altering the deposition mechanism. At 70°C could not observe any notable change in pH during the deposition after several hours of

reaction time. The initial pH drop is related to heating up the solution to 70°C. Increase of the pH in several single points is most likely due to experimental artefacts. Samples of SnO_2 on FTO with 1, 2 and 3 CBD cycles and 1h reaction time each were prepared for device fabrication.

Sequential slot-die coating is used to grow triple-cation perovskite films onto the CBD SnO_2 layers. This two-step deposition process previously developed in our laboratory allows the deposition of uniform and pinhole free perovskite layers.[27] During the process, an intermediate layer containing CsI and PbI_2 is deposited by a first slot-die coating step, then vacuum treated to remove excess solvent and thereafter converted to perovskite applying the organic cations solution on top using a second slot-die coating step as schematically described in Figure 2a.

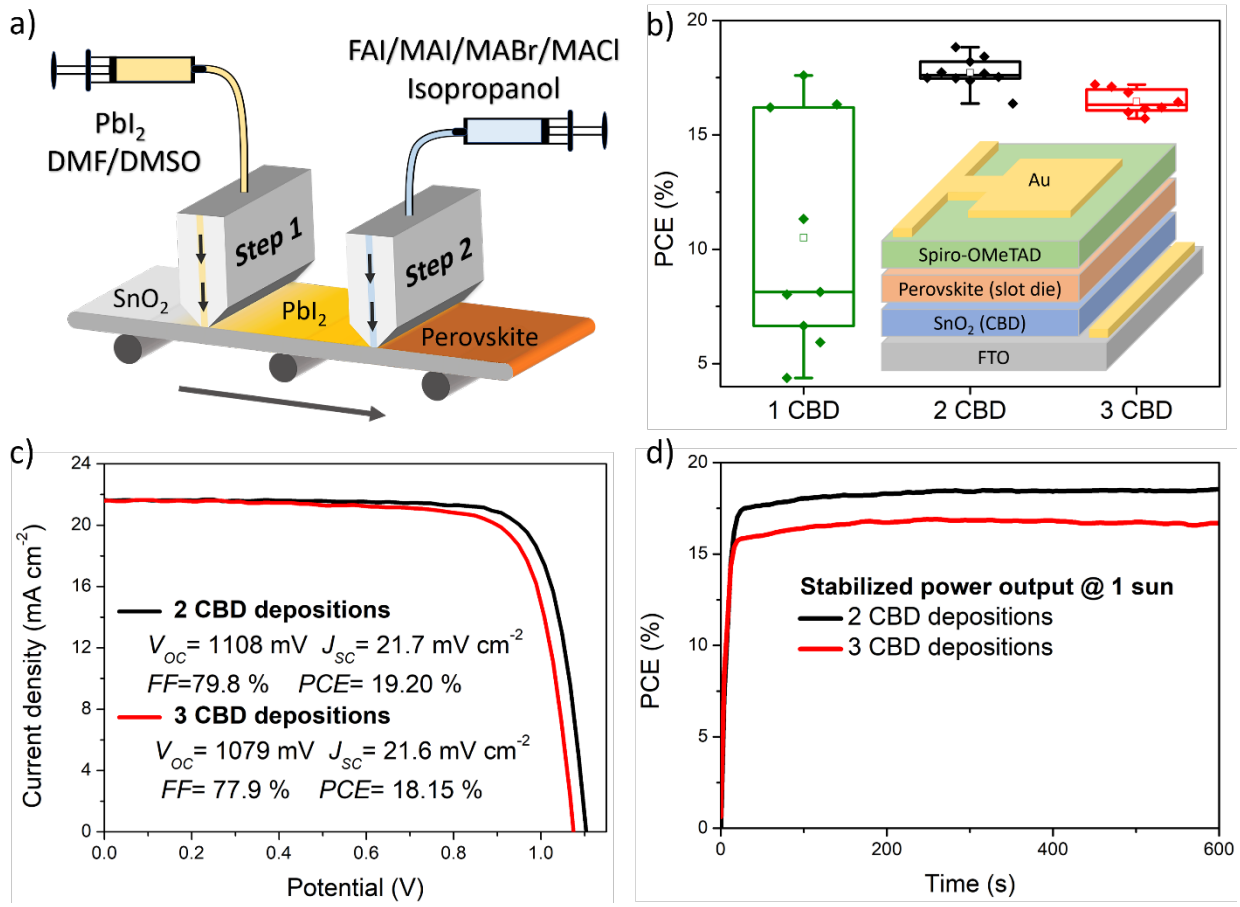

Figure 2 Fabrication of small area (0.09 cm^2) perovskite devices: a) schematic illustration of the perovskite deposition on the SnO_2 layers by sequential slot-die-coating. b) Efficiency distribution of PSC fabricated on SnO_2 layers produced using 1,2 and 3 CBD cycles. The inset displays a schematic drawing of the device architecture. c) Current-voltage curves (reverse scan) of the champion devices on SnO_2 layers from 2 and 3 chemical bath depositions. d) Stabilized power output measured at 1 sun.

This layer was then thermally annealed at 150°C for 15 min. Detailed experimental information on the perovskite deposition can be found in the Supporting Information. The perovskite used in this work is $Cs_{0.05}MA_{0.4}$ $FA_{0.55}Pb(I_{0.96}Br_{0.04})_3$ assuming stochiometric conversion of the precursors and MACl is used as an additive to promote grain growth. The perovskite has been deposited on the 5 x 10 cm^2 CBD-SnO_2 substrates, which were then cut down to individual devices before applying Spiro-OMeTAD as the hole extracting layer using spin-coating. Devices were fabricated on SnO_2 layers that have been grown using 1, 2 or 3 one hour-long subsequential CBD reactions as described above. This allows for optimizing the ideal thickness of the CBD SnO_2 in terms of device performances, which results are summarized in Figure 2b and Figure S5. The reported parameters are extracted from current-voltage (J-V) measurements performed in reverse scan direction under 1 sun simulated sunlight (100 mW cm^{-2}). We found that one CBD bath alone is not enough for reproducibly fabricating efficient perovskite devices as a large spread in device efficiencies can be observed. These results are consistent with the incomplete hole blocking observed in the electrochemical experiments above. Indeed, the loss in Voc and FF likely arising from non-radiative recombination at the SnO_2/perovskite interface are consistent with an incomplete coverage of the FTO surface. With two and three CBD on the other hand, a very narrow distribution in efficiency and thus high reproducibility can be observed. Two CBD result in the

optimum SnO_2 thickness, yielding the best device results. The reverse IV-curves of the champion devices with two and three CBD SnO_2 layers are displayed in Figure 2c. PCEs of 19.2 % and 18.2 % could be obtained using SnO_2 with 2 and 3 deposition cycles respectively. These values were further confirmed measuring the stabilized power output of the PSCs under 1 sun constant illumination using maximum power point tracking (MPPT) as shown in Figure 2d. Stabilized PCE values after 10 minutes of MPPT result in 18.6 % and 16.7 % for 2 and 3 SnO_2 CBDs respectively. Furthermore, we found that the integrated photocurrent from external quantum efficiency (EQE) measurements of the champion device (20.8 mA cm^{-2}) shown in Figure S6 closely matches with the current density measured from J-V curves (21.7 mA cm^{-2}). With thicker SnO_2 layers after 3 CBDs, the main difference in device performance stems from a decrease in open-circuit voltage (Voc) and fill factor (FF). We speculate that the lowering in efficiency with 3 CBD cycles is two-fold. On one hand the larger number of aggregates of SnO_2 nanoparticles observed from SEM images on the substrate surface compromises uniformity of the PSC. On the other hand, a thicker SnO_2 layer exhibits a larger series resistance that negatively affects the FF of the PSCs.

To investigate the perovskite growth on the optimized CBD SnO_2 layers (2 deposition cycles) we performed STEM analysis on complete PSC devices and SEM-CL on half cells (FTO/SnO_2/perovskite). Figure 3a shows the cross section of a perovskite device acquired using high-angle annular dark-field imaging (HAADF). The around 200 nm thick lamella utilized in this experiment was obtained by slow ion milling of the PSC sample. The different layers of the PSC are clearly visible and from the HAADF image and we estimate the thickness of the SnO_2 layer to be around 20 nm. The around 350 nm thick perovskite layer consists of well-defined grains having a diameter up to 500 nm with grain boundaries clearly visible. The voids appearing in between the grain boundaries are thereby most likely due to electron-beam-induced shrinking of the perovskite

grains as reported previously.[35] The elemental distribution within the cross-section lamella was investigated by Energy dispersive X-ray spectroscopy (EDS). EDS maps for relevant elements are displayed in Figure 3b. Distinguishing the SnO_2 layer from the underlaying FTO due to the very similar composition turned out to be difficult. However, we found evidence for small SnO_2 nanoparticles being present on the surface. Looking at distribution of the main elements present in the perovskite layer (Pb, I, Br) we can observe a very homogeneous distribution throughout the grains. This indicates a complete conversion of the perovskite during the sequential deposition with no remaining PbI_2 clusters present in the bulk. From XRD diffraction shown in Figure 3c we observe the formation of the cubic perovskite phase with strong preferred orientation of the crystallites along the <100> crystallographic direction. A small peak at around 12.6° 2θ indicates the presence of unreacted PbI_2 in the layer. To investigate the top surface of the perovskite film we performed cathodoluminescence (CL) measurements (Figure 3d). CL maps were acquired at low temperature (170 K) to increase the luminescence intensity and to limit the beam damage, indicated by a broad emission around 630 nm at room temperature (Figure S7). The luminescence signal arising from the localized excitation of the perovskite layer is recorded over a surface of 50 μm^2. The distribution of the perovskite signal is uniform. On the other hand, the SEM image overlaid with the contribution of PbI_2 CL emission reveals the presence of small lead iodide clusters on the surface (Figure 3d). PbI_2 can also be observed on the surface of the perovskite film using backscattered electron microscopy images (Figure S7), and are commonly occurring in sequentially deposited perovskite.[36]

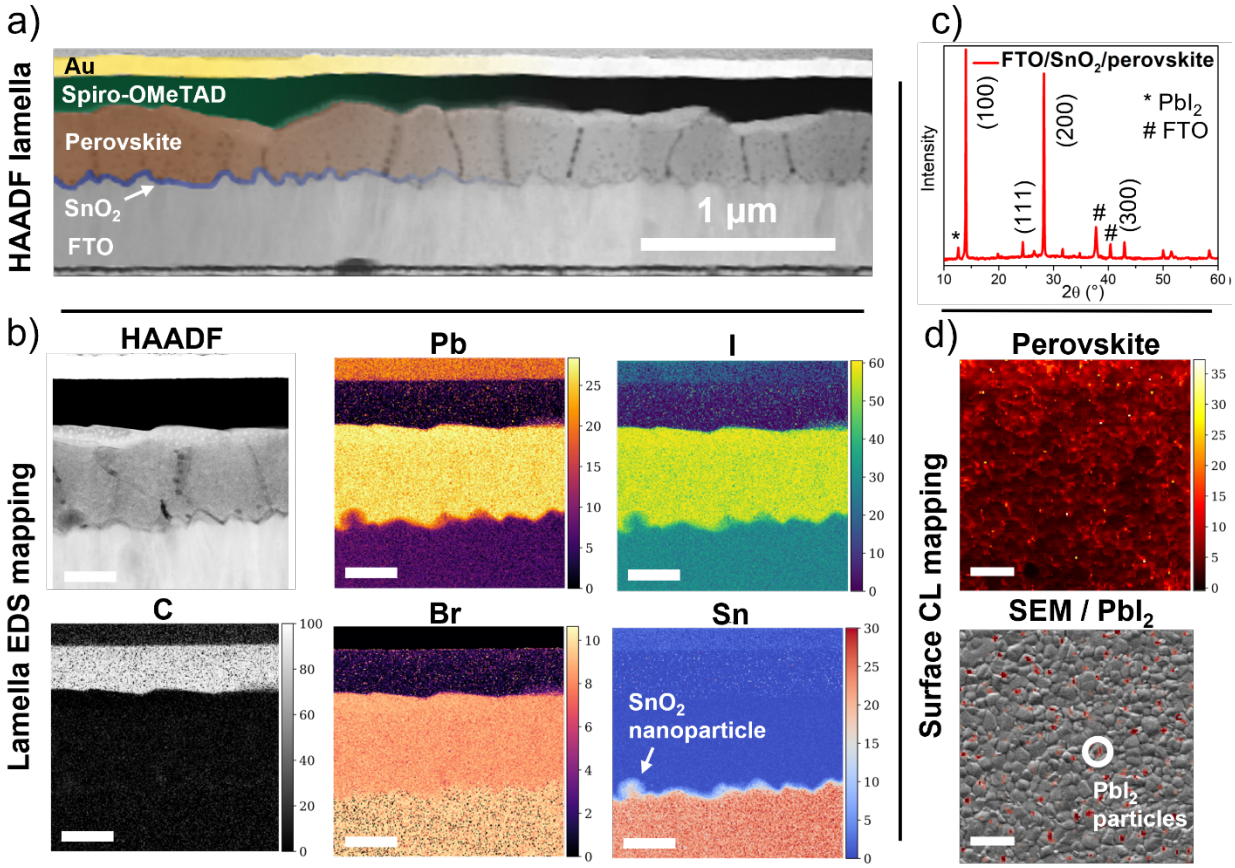

Figure 3 Characterization of the PSC: (a) High-angle annular dark-field imaging (HAADF) recorded on a STEM system showing the cross-section of a full perovskite device. The measured ~200 nm thick lamella has been prepared by ion milling. (b) Cross-section EDS mapping performed on the lamella highlighting the quantified distribution of relevant elements in the device stack in atomic %. Scale bar at 200 nm. (c) X-ray diffraction of the perovskite layer deposited on FTO/SnO_2. (d) Surface cathodoluminescence (CL) mapping performed on half devices (FTO/SnO_2/perovskite). Map of the emission (750-800nm) originating from the perovskite phase (top). Map of the PbI_2 emission (475-525nm) overlaid on the corresponding SEM image revealing the presence of lead iodide particles on the surface. Scale bar at 2 μm.

To demonstrate the use of CBD deposited SnO_2 as simple and reliable deposition method for upscaling PSCs to larger device areas, mini-modules were fabricated. Thereby, mini-modules with

12 cm^2 aperture area deposited on 5x10 cm^2 substrates were used to fully optimize the scribing process. Finally, mini-modules with an aperture area of 40 cm^2 deposited on 10 x 10 cm^2 substrates were fabricated utilizing the previously optimized processing parameters. Laser ablation is used for connecting individual perovskite sub cells into modules. A schematic cross-sectional view on the mini-model design is shown in Figure 4a. This method requires three subsequent scribing steps, conventionally dubbed P_1, P_2, P_3.[37] The mini-modules fabricated in this work consist of sub cells connected in series, that are 5 mm wide. The fraction of the actual photo active area in a module depends on the dead cell width (w_d) generated by the laser scribing as well as the active cell width (w_a) and is often expressed as the geometrical factor $G_{FF} = w_a / (w_a + w_d)$. In this work wd is around 300 μm as observed from profilometer images of the laser scribes, resulting in a G_{FF} of around 94 %. The quality of the interconnection of the individual sub cells achieved with P2 is of great importance for the module efficiency. The P2 laser power needs to be carefully tuned to fully remove all the layers including the SnO_2 ETL without damaging the underlaying TCO to assure a good electrical connection. We found that using a P2 laser power of around 12.7 W, previously optimized for compact titania / tin oxide bilayers[27], is too strong for the current SnO_2 based device stack. This could be observed from cross-sectional SEM images showing a complete removal of the FTO in the center of the P2 scribe, compromising the electrical transfer. (Figure S8) Consequently mini-modules fabricated with high P2 laser power settings demonstrate low efficiency (Table S1). The main photovoltaic parameter affected is the fill factor due to the increased series resistance originating from the insufficient Au/FTO connection in the P2 scribe. Optimized P2 laser power settings of 10.8 W on the other hand reveals only slight damage to the FTO in the center of the scribe, allowing for a superior contact. Due to the Gaussian shape of the laser beam, the layers in the solar cell stack are removed gradually towards the center of the laser

scribe as shown in Figure S9, allowing for complete removal of the SnO_2 only close to the middle. Previous studies show that the ideal contact length of gold with the TCO is in the range of 10 μm to 20 μm.[30] The performance of the fabricated mini-modules is investigated using reverse current-voltage (IV) sweeps shown in Figure 4c. We observed a power conversion efficiency of 16.0 % (17.0 % on active area) for the best 12 cm^2 mini-module with an open-circuit voltage (V_{oc}) of 6.35 V, short-circuit current (J_{sc}) of 3.52 mA cm^{-2} and a fill factor (FF) of 71.8 %. Mini-modules fabricated with a 40 cm^2 aperture area displayed a maximum PCE of 17.0% (18.1 % on active area) with a V_{oc} of 17.61 V, J_{sc} of 1.31 mA cm^{-2} and an FF of 73.5 %. These values are among the highest for slot-die deposited perovskite mini-modules and a detailed comparison with other reports is outlined in Table S2. Stabilized power output using maximum power point tracking is shown in Figure S10, demonstrating a stabilized efficiency of around 15% (16 % on active area) for the 12 cm^2 and around 16.5 % (17.6 % on active area) for the 40 cm^2 aperture area champion modules. The slightly higher efficiency of the larger mini-module is attributed to the improved processing protocols developed during the 12 cm^2 module fabrication process. Most importantly, we demonstrate that the efficiency-drop from small devices (PCE = 19.2%) with 0.09 cm^2 active area towards mini-modules (PCE=18.1%) with 37.6 cm^2 active area is only around 6 %. We believe that the relatively small drop in efficiency from small cells to 40 cm^2 modules is due to the homogeneous deposition of the SnO_2 layer and of the perovskite layer due to the use of scalable techniques. The uniformity in terms of thickness is expected to be much better with chemical bath deposition and slot-die coating compared to spin-coating. The second reason is the careful optimization of the P2 laser scribing, which allowed for low contact resistance and thus high fill factors in the mini-modules. These results are very promising in terms of upscaling of the perovskite technology to larger module sizes.

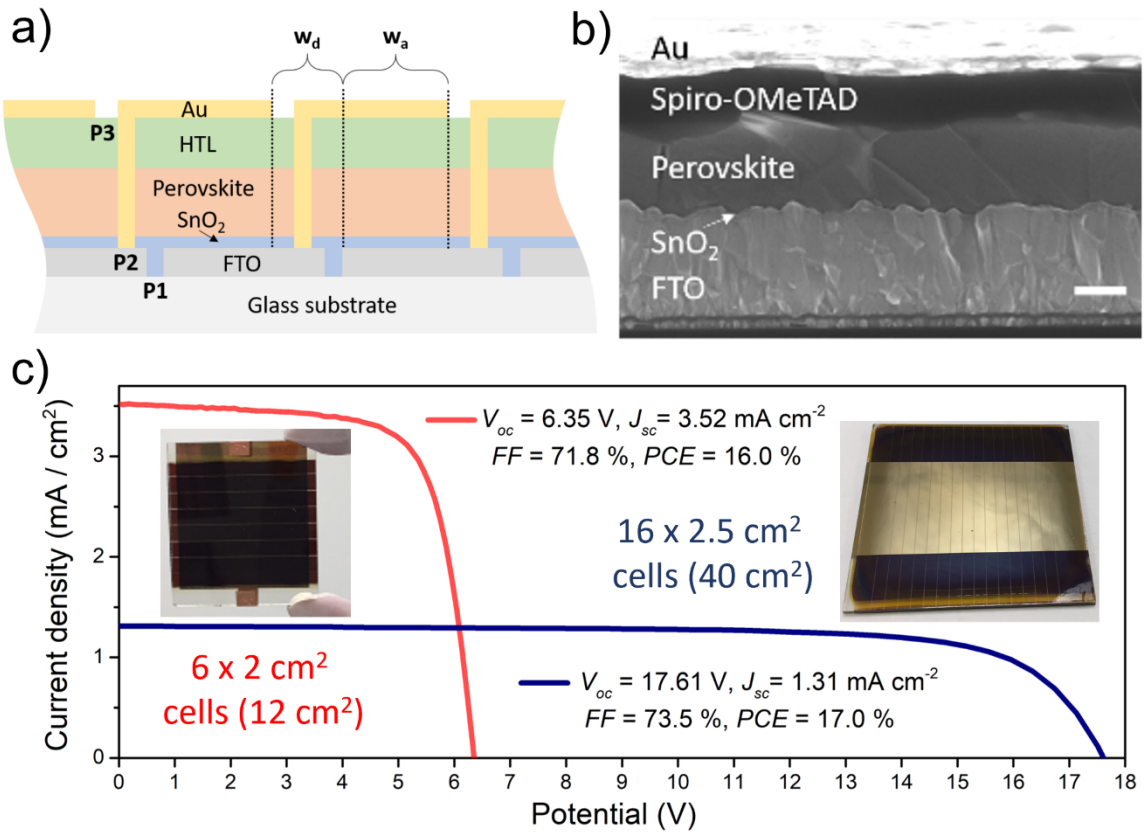

Figure 4 Design and characterization of mini-modules with 12 cm^2 aperture area: a) schematic illustration of the serial interconnection of perovskite sub cells by subsequent P1, P2 and P3 laser scribing steps. Active cell width and dead cell width within the module are indicated by w_a and w_d respectively. b) Cross sectional SEM image of the perovskite mini-module. Scale bar at 200 nm. c) Current-voltage (IV) curves of the perovskite modules having 12cm^2 aperture area (red) and 40 cm^2 aperture area (blue).

In summary this work outlines strategies in depositing uniform SnO_2 layers by chemical bath deposition to be used as electron transport layer in efficient perovskite solar devices. Using an in-situ quartz micro-balance setup coupled with a pH probe, the SnO_2 deposition process could be closely followed. Oxygen is found to play a significant role in producing solubilized active $Sn(OH)_4$ precursor species during solution aging that further decompose to SnO_2 during the CBD

at 70°C. Sequential slot-die-deposition is presented as an effective method to produce high quality perovskite films onto the CBD SnO_2 layers. Cross-sectional STEM/EDX measurements as well as SEM/CL surface analysis reveal the growth of uniform perovskite films. Finally, laboratory devices with a PCE of over 19% and mini-modules with a PCE of 16 % for 12 cm^2 and 17% for 40 cm^2 could be achieved. Overall, the combination of CBD deposited SnO_2 together with sequentially slot-die-coated perovskite has demonstrated great potential for upscaling the perovskite technology to larger module size.

ASSOCIATED CONTENT

Supporting Information. Experimental procedures, supplementary figures and tables.

Notes

The authors declare no competing financial interest.

ACKNOWLEDGMENT

This project was supported by the French Government in the frame of the program of investment for the future (Programme d'Investissement d'Avenir - Agence Nationale de la Recherche, Grant No. ANR-IEED-002-01). Dr. Daniel Lincot is acknowledged for fruitful discussions on the SnO_2 deposition mechanism.

REFERENCES

(1) Jeong, J.; Kim, M.; Seo, J.; Lu, H.; Ahlawat, P.; Mishra, A.; Yang, Y.; Hope, M. A.; Eickemeyer, F. T.; Kim, M.; Yoon, Y. J.; Choi, I. W.; Darwich, B. P.; Choi, S. J.; Jo, Y.; Lee, J. H.; Walker, B.; Zakeeruddin, S. M.; Emsley, L.; Rothlisberger, U.; Hagfeldt, A.; Kim, D. S.; Grätzel, M.; Kim, J. Y. Pseudo-Halide Anion Engineering for α-FAPbI 3 Perovskite Solar Cells. *Nature* **2021**, 1–5. https://doi.org/10.1038/s41586-021-03406-5.

(2) Best Research-Cell Efficiency Chart | Photovoltaic Research | NREL https://www.nrel.gov/pv/cell-efficiency.html (accessed 2019 -06 -25).

(3) Yoo, J. J.; Seo, G.; Chua, M. R.; Park, T. G.; Lu, Y.; Rotermund, F.; Kim, Y.-K.; Moon, C. S.; Jeon, N. J.; Correa-Baena, J.-P.; Bulović, V.; Shin, S. S.; Bawendi, M. G.; Seo, J. Efficient Perovskite Solar Cells via Improved Carrier Management. *Nature* **2021**, *590* (7847), 587–593. https://doi.org/10.1038/s41586-021-03285-w.

(4) De Wolf, S.; Holovsky, J.; Moon, S.-J.; Löper, P.; Niesen, B.; Ledinsky, M.; Haug, F.-J.; Yum, J.-H.; Ballif, C. Organometallic Halide Perovskites: Sharp Optical Absorption Edge and Its Relation to Photovoltaic Performance. *J. Phys. Chem. Lett.* **2014**, *5* (6), 1035–1039. https://doi.org/10.1021/jz500279b.

(5) Herz, L. M. Charge-Carrier Mobilities in Metal Halide Perovskites: Fundamental Mechanisms and Limits. *ACS Energy Lett.* **2017**, *2* (7), 1539–1548. https://doi.org/10.1021/acsenergylett.7b00276.

(6) Zhang, F.; Yang, B.; Li, Y.; Deng, W.; He, R. Extra Long Electron–Hole Diffusion Lengths in CH3NH3PbI3−xClx Perovskite Single Crystals. *J. Mater. Chem. C* **2017**, *5* (33), 8431–8435. https://doi.org/10.1039/C7TC02802D.

(7) Kim, J.; Lee, S.-H.; Lee, J. H.; Hong, K.-H. The Role of Intrinsic Defects in Methylammonium Lead Iodide Perovskite. *J. Phys. Chem. Lett.* **2014**, *5* (8), 1312–1317. https://doi.org/10.1021/jz500370k.

(8) Li, J.; Dagar, J.; Shargaieva, O.; Flatken, M. A.; Köbler, H.; Fenske, M.; Schultz, C.; Stegemann, B.; Just, J.; Többens, D. M.; Abate, A.; Munir, R.; Unger, E. 20.8% Slot-Die Coated MAPbI3 Perovskite Solar Cells by Optimal DMSO-Content and Age of 2-ME Based Precursor Inks. *Advanced Energy Materials* **2021**, *11* (10), 2003460. https://doi.org/10.1002/aenm.202003460.

(9) Gao, L.; Huang, K.; Long, C.; Zeng, F.; Liu, B.; Yang, J. Fully Slot-Die-Coated Perovskite Solar Cells in Ambient Condition. *Appl. Phys. A* **2020**, *126* (6), 452. https://doi.org/10.1007/s00339-020-03628-w.

(10) Tang, M.-C.; Fan, Y.; Barrit, D.; Chang, X.; Dang, H. X.; Li, R.; Wang, K.; Smilgies, D.-M.; Liu, S. (Frank); Wolf, S. D.; Anthopoulos, T. D.; Zhao, K.; Amassian, A. Ambient Blade Coating of Mixed Cation, Mixed Halide Perovskites without Dripping: In Situ Investigation and Highly Efficient Solar Cells. *J. Mater. Chem. A* **2020**, *8* (3), 1095–1104. https://doi.org/10.1039/C9TA12890E.

(11) Hu, H.; Ren, Z.; Fong, P. W. K.; Qin, M.; Liu, D.; Lei, D.; Lu, X.; Li, G. Room-Temperature Meniscus Coating of >20% Perovskite Solar Cells: A Film Formation Mechanism Investigation. *Advanced Functional Materials* **2019**, *29* (25), 1900092. https://doi.org/10.1002/adfm.201900092.
(12) Chang, X.; Fang, J.; Fan, Y.; Luo, T.; Su, H.; Zhang, Y.; Lu, J.; Tsetseris, L.; Anthopoulos, T. D.; Liu, S. (Frank); Zhao, K. Printable CsPbI3 Perovskite Solar Cells with PCE of 19% via an Additive Strategy. *Advanced Materials* **2020**, *32* (40), 2001243. https://doi.org/10.1002/adma.202001243.
(13) Deng, Y.; Xu, S.; Chen, S.; Xiao, X.; Zhao, J.; Huang, J. Defect Compensation in Formamidinium–Caesium Perovskites for Highly Efficient Solar Mini-Modules with Improved Photostability. *Nat Energy* **2021**, *6* (6), 633–641. https://doi.org/10.1038/s41560-021-00831-8.
(14) Bishop, J. E.; Read, C. D.; Smith, J. A.; Routledge, T. J.; Lidzey, D. G. Fully Spray-Coated Triple-Cation Perovskite Solar Cells. *Scientific Reports* **2020**, *10* (1), 6610. https://doi.org/10.1038/s41598-020-63674-5.
(15) Mathies, F.; List-Kratochvil, E. J. W.; Unger, E. L. Advances in Inkjet-Printed Metal Halide Perovskite Photovoltaic and Optoelectronic Devices. *Energy Technology* **2020**, *8* (4), 1900991. https://doi.org/10.1002/ente.201900991.
(16) NREL. *Champion Photovoltaic Module Efficiency Chart: Https://Www.Nrel.Gov/Pv/Assets/Pdfs/Champion-Module-Efficiencies.Pdf (Accessed: September 2021).*
(17) Anaraki, E. H.; Kermanpur, A.; Steier, L.; Domanski, K.; Matsui, T.; Tress, W.; Saliba, M.; Abate, A.; Grätzel, M.; Hagfeldt, A.; Correa-Baena, J.-P. Highly Efficient and Stable Planar Perovskite Solar Cells by Solution-Processed Tin Oxide. *Energy Environ. Sci.* **2016**, *9* (10), 3128–3134. https://doi.org/10.1039/C6EE02390H.
(18) Liang, C.; Wu, Z.; Li, P.; Fan, J.; Zhang, Y.; Shao, G. Chemical Bath Deposited Rutile TiO2 Compact Layer toward Efficient Planar Heterojunction Perovskite Solar Cells. *Applied Surface Science* **2017**, *391*, 337–344. https://doi.org/10.1016/j.apsusc.2016.06.171.
(19) Bae, D. A Comparative Study of (Cd,Zn)S Buffer Layers for Cu(In,Ga)Se2 Solar Panels Fabricated by Chemical Bath and Surface Deposition Methods. *Materials* **2020**, *13* (7), 1622. https://doi.org/10.3390/ma13071622.
(20) Kim, S.; Yun, Y. J.; Kim, T.; Lee, C.; Ko, Y.; Jun, Y. Hydrolysis-Regulated Chemical Bath Deposition of Tin-Oxide-Based Electron Transport Layers for Efficient Perovskite Solar Cells with a Reduced Potential Loss. *Chemistry of Materials* **2021**. https://doi.org/10.1021/acs.chemmater.1c02101.
(21) Min, H.; Lee, D. Y.; Kim, J.; Kim, G.; Lee, K. S.; Kim, J.; Paik, M. J.; Kim, Y. K.; Kim, K. S.; Kim, M. G.; Shin, T. J.; Il Seok, S. Perovskite Solar Cells with Atomically Coherent Interlayers on SnO2 Electrodes. *Nature* **2021**, *598* (7881), 444–450. https://doi.org/10.1038/s41586-021-03964-8.
(22) Tong, G.; Ono, L. K.; Liu, Y.; Zhang, H.; Bu, T.; Qi, Y. Up-Scalable Fabrication of SnO2 with Multifunctional Interface for High Performance Perovskite Solar Modules. *Nano-Micro Lett.* **2021**, *13* (1), 155. https://doi.org/10.1007/s40820-021-00675-7.
(23) Bernard, S.; Jutteau, S.; Mejaouri, S.; Cacovich, S.; Zimmerman, I.; Yaiche, A.; Gbegnon, S.; Loisnard, D.; Collin, S.; Duchatelet, A.; Sauvage, F.; Rousset, J. One-Step Slot-Die Coating Deposition of Wide-Bandgap Perovskite Absorber for Highly Efficient Solar Cells. *Solar RRL n/a* (n/a). https://doi.org/10.1002/solr.202100391.

(24) Burkitt, D.; Swartwout, R.; McGettrick, J.; Greenwood, P.; Beynon, D.; Brenes, R.; Bulović, V.; Watson, T. Acetonitrile Based Single Step Slot-Die Compatible Perovskite Ink for Flexible Photovoltaics. *RSC Adv.* **2019**, *9* (64), 37415–37423. https://doi.org/10.1039/C9RA06631D.
(25) Ding, J.; Han, Q.; Ge, Q.-Q.; Xue, D.-J.; Ma, J.-Y.; Zhao, B.-Y.; Chen, Y.-X.; Liu, J.; Mitzi, D. B.; Hu, J.-S. Fully Air-Bladed High-Efficiency Perovskite Photovoltaics. *Joule* **2019**, *3* (2), 402–416. https://doi.org/10.1016/j.joule.2018.10.025.
(26) Huang, Y.-C.; Li, C.-F.; Huang, Z.-H.; Liu, P.-H.; Tsao, C.-S. Rapid and Sheet-to-Sheet Slot-Die Coating Manufacture of Highly Efficient Perovskite Solar Cells Processed under Ambient Air. *Solar Energy* **2019**, *177*, 255–261. https://doi.org/10.1016/j.solener.2018.11.020.
(27) Zimmermann, I.; Atem, M. A.; Fournier, O.; Bernard, S.; Jutteau, S.; Lombez, L.; Rousset, J. Sequentially Slot-Die-Coated Perovskite for Efficient and Scalable Solar Cells. *Advanced Materials Interfaces n/a* (n/a), 2100743. https://doi.org/10.1002/admi.202100743.
(28) Burkitt, D.; Searle, J.; Worsley, D. A.; Watson, T. Sequential Slot-Die Deposition of Perovskite Solar Cells Using Dimethylsulfoxide Lead Iodide Ink. *Materials (Basel)* **2018**, *11* (11). https://doi.org/10.3390/ma11112106.
(29) Yang, M.; Kim, D. H.; Klein, T. R.; Li, Z.; Reese, M. O.; Tremolet de Villers, B. J.; Berry, J. J.; van Hest, M. F. A. M.; Zhu, K. Highly Efficient Perovskite Solar Modules by Scalable Fabrication and Interconnection Optimization. *ACS Energy Lett.* **2018**, *3* (2), 322–328. https://doi.org/10.1021/acsenergylett.7b01221.
(30) Rakocevic, L.; Gehlhaar, R.; Merckx, T.; Qiu, W.; Paetzold, U. W.; Fledderus, H.; Poortmans, J. Interconnection Optimization for Highly Efficient Perovskite Modules. *IEEE Journal of Photovoltaics* **2017**, *7* (1), 404–408. https://doi.org/10.1109/JPHOTOV.2016.2626144.
(31) Peres, L.; Bou, A.; Cornille, C.; Barakel, D.; Torchio, P. Work Function Measurement of Multilayer Electrodes Using Kelvin Probe Force Microscopy. *J. Phys. D: Appl. Phys.* **2017**, *50* (13), 13LT01. https://doi.org/10.1088/1361-6463/aa5f4a.
(32) Liu, H.; Zhang, W.; Yu, H.; Gao, L.; Song, Z.; Xu, S.; Li, M.; Wang, Y.; Song, H.; Tang, J. Solution-Processed Gas Sensors Employing SnO2 Quantum Dot/MWCNT Nanocomposites. *ACS Appl. Mater. Interfaces* **2016**, *8* (1), 840–846. https://doi.org/10.1021/acsami.5b10188.
(33) House, C. I.; Kelsall, G. H. Potential—PH Diagrams for the Sn/H2O□Cl System. *Electrochimica Acta* **1984**, *29* (10), 1459–1464. https://doi.org/10.1016/0013-4686(84)87028-0.
(34) Filson, G. W.; Walton, J. H. The Autoxidation of Stannous and Cuprous Chlorides by Air. *The Journal of Physical Chemistry* **2002**. https://doi.org/10.1021/j150332a034.
(35) Yadavalli, S. K.; Chen, M.; Hu, M.; Dai, Z.; Zhou, Y.; Padture, N. P. Electron-Beam-Induced Cracking in Organic-Inorganic Halide Perovskite Thin Films. *Scripta Materialia* **2020**, *187*, 88–92. https://doi.org/10.1016/j.scriptamat.2020.05.062.
(36) Li, Q.; Zhao, Y.; Zhou, W.; Han, Z.; Fu, R.; Lin, F.; Yu, D.; Zhao, Q. Halogen Engineering for Operationally Stable Perovskite Solar Cells via Sequential Deposition. *Advanced Energy Materials* **2019**, *9* (46), 1902239. https://doi.org/10.1002/aenm.201902239.
(37) Palma, A. L.; Matteocci, F.; Agresti, A.; Pescetelli, S.; Calabrò, E.; Vesce, L.; Christiansen, S.; Schmidt, M.; Carlo, A. D. Laser-Patterning Engineering for Perovskite Solar Modules

With 95% Aperture Ratio. *IEEE Journal of Photovoltaics* **2017**, *7* (6), 1674–1680. https://doi.org/10.1109/JPHOTOV.2017.2732223.